

THE ATACAMA COSMOLOGY TELESCOPE: SUNYAEV-ZEL'DOVICH SELECTED GALAXY CLUSTERS AT 148 GHz IN THE 2008 SURVEY

TOBIAS A. MARRIAGE^{1,2}, VIVIANA ACQUAVIVA^{3,1}, PETER A. R. ADE⁴, PAULA AGUIRRE⁵, MANDANA AMIRI⁶, JOHN WILLIAM APPEL⁷, L. FELIPE BARRIENTOS⁵, ELIA S. BATTISTELLI^{8,6}, J RICHARD BOND⁹, BEN BROWN¹⁰, BRYCE BURGER⁶, JAY CHERVENAK¹¹, SUDEEP DAS^{12,7,1}, MARK J. DEVLIN¹³, SIMON R. DICKER¹³, W. BERTRAND DORIESE¹⁴, JOANNA DUNKLEY^{15,7,1}, ROLANDO DÜNNER⁵, THOMAS ESSINGER-HILEMAN⁷, RYAN P. FISHER⁷, JOSEPH W. FOWLER^{14,7}, AMIR HAJIAN^{9,1,7}, MARK HALPERN⁶, MATTHEW HASSELFIELD⁶, CARLOS HERNÁNDEZ-MONTEAGUDO¹⁶, GENE C. HILTON¹⁴, MATT HILTON^{17,18}, ADAM D. HINCKS⁷, RENÉE HLOZEK¹⁵, KEVIN M. HUFFENBERGER¹⁹, DAVID HANDEL HUGHES²⁰, JOHN P. HUGHES³, LEOPOLDO INFANTE⁵, KENT D. IRWIN¹⁴, JEAN BAPTISTE JUIN⁵, MADHURI KAUL¹³, JEFF KLEIN¹³, ARTHUR KOSOWSKY¹⁰, JUDY M LAU^{21,22,7}, MICHELE LIMON^{23,13,7}, YEN-TING LIN^{24,1,5}, ROBERT H. LUPTON¹, DANICA MARSDEN¹³, KRISTA MARTOCCI^{25,7}, PHIL MAUSKOPF⁴, FELIPE MENANTEAU³, KAVILAN MOODLEY^{17,18}, HARVEY MOSELEY¹¹, CALVIN B NETTERFIELD²⁶, MICHAEL D. NIEMACK^{14,7}, MICHAEL R. NOLTA⁹, LYMAN A. PAGE⁷, LUCAS PARKER⁷, BRUCE PARTRIDGE²⁷, HERNAN QUINTANA⁵, ERIK D. REESE¹³, BETH REID^{28,7}, NEELIMA SEHGAL²¹, BLAKE D. SHERWIN⁷, JON SIEVERS⁹, DAVID N. SPERGEL¹, SUZANNE T. STAGGS⁷, DANIEL S. SWETZ^{13,14}, ERIC R. SWITZER^{25,7}, ROBERT THORNTON^{13,29}, HY TRAC^{30,31}, CAROLE TUCKER⁴, RYAN WARE¹⁷, GRANT WILSON³², ED WOLLACK¹¹, YUE ZHAO⁷

Accepted in ApJ

ABSTRACT

We report on twenty-three clusters detected blindly as Sunyaev-Zel'dovich (SZ) decrements in a 148 GHz, 455 square-degree map of the southern sky made with data from the Atacama Cosmology Telescope 2008 observing season. All SZ detections announced in this work have confirmed optical counterparts. Ten of the clusters are new discoveries. One newly discovered cluster, ACT-CL J0102-4915, with a redshift of 0.75 (photometric), has an SZ decrement comparable to the most massive systems at lower redshifts. Simulations of the cluster recovery method reproduce the sample purity measured by optical follow-up. In particular, for clusters detected with a signal-to-noise ratio greater than six, simulations are consistent with optical follow-up that demonstrated this subsample is 100% pure. The simulations further imply that the total sample is 80% complete for clusters with mass in excess of 6×10^{14} solar masses referenced to the cluster volume characterized by five hundred times the critical density. The Compton y – X-ray luminosity mass comparison for the eleven best detected clusters visually agrees with both self-similar and non-adiabatic, simulation-derived scaling laws.

Subject headings: Surveys – Cosmology:observations – Radio continuum: general – Galaxies: clusters: general – cosmic background radiation

¹ Department of Astrophysical Sciences, Peyton Hall, Princeton University, Princeton, NJ USA 08544

² Current address: Dept. of Physics and Astronomy, Johns Hopkins University, 3400 N. Charles St., Baltimore, MD 21218-2686

³ Department of Physics and Astronomy, Rutgers, The State University of New Jersey, Piscataway, NJ USA 08854-8019

⁴ School of Physics and Astronomy, Cardiff University, The Parade, Cardiff, Wales, UK CF24 3AA

⁵ Departamento de Astronomía y Astrofísica, Facultad de Física, Pontificia Universidad Católica, Casilla 306, Santiago 22, Chile

⁶ Department of Physics and Astronomy, University of British Columbia, Vancouver, BC, Canada V6T 1Z4

⁷ Joseph Henry Laboratories of Physics, Jadwin Hall, Princeton University, Princeton, NJ, USA 08544

⁸ Department of Physics, University of Rome “La Sapienza”, Piazzale Aldo Moro 5, I-00185 Rome, Italy

⁹ Canadian Institute for Theoretical Astrophysics, University of Toronto, Toronto, ON, Canada M5S 3H8

¹⁰ Department of Physics and Astronomy, University of Pittsburgh, Pittsburgh, PA, USA 15260

¹¹ Code 553/665, NASA/Goddard Space Flight Center, Greenbelt, MD, USA 20771

¹² Berkeley Center for Cosmological Physics, LBL and Department of Physics, University of California, Berkeley, CA, USA 94720

¹³ Department of Physics and Astronomy, University of Pennsylvania, 209 South 33rd Street, Philadelphia, PA, USA 19104

¹⁴ NIST Quantum Devices Group, 325 Broadway Mailcode 817.03, Boulder, CO, USA 80305

¹⁵ Department of Astrophysics, Oxford University, Oxford, UK OX1 3RH

¹⁶ Max Planck Institut für Astrophysik, Postfach 1317, D-85741

Garching bei München, Germany

¹⁷ Astrophysics and Cosmology Research Unit, School of Mathematical Sciences, University of KwaZulu-Natal, Durban, 4041, South Africa

¹⁸ Centre for High Performance Computing, CSIR Campus, 15 Lower Hope St., Rosebank, Cape Town, South Africa

¹⁹ Department of Physics, University of Miami, Coral Gables, FL, USA 33124

²⁰ Instituto Nacional de Astrofísica, Óptica y Electrónica (INAOE), Tonantzintla, Puebla, Mexico

²¹ Kavli Institute for Particle Astrophysics and Cosmology, Stanford University, Stanford, CA, USA 94305-4085

²² Department of Physics, Stanford University, Stanford, CA, USA 94305-4085

²³ Columbia Astrophysics Laboratory, 550 W. 120th St. Mail Code 5247, New York, NY USA 10027

²⁴ Institute for the Physics and Mathematics of the Universe, The University of Tokyo, Kashiwa, Chiba 277-8568, Japan

²⁵ Kavli Institute for Cosmological Physics, 5620 South Ellis Ave., Chicago, IL, USA 60637

²⁶ Department of Physics, University of Toronto, 60 St. George Street, Toronto, ON, Canada M5S 1A7

²⁷ Department of Physics and Astronomy, Haverford College, Haverford, PA, USA 19041

²⁸ Institut de Ciències del Cosmos (ICC), University of Barcelona, Barcelona 08028, Spain

²⁹ Department of Physics, West Chester University of Pennsylvania, West Chester, PA, USA 19383

³⁰ Department of Physics, Carnegie Mellon University, Pittsburgh, PA 15213

1. INTRODUCTION

Measuring the redshift evolution of the mass function of galaxy clusters provides powerful constraints on cosmological parameters, complementary to those obtained from different measurements, such as the angular power spectrum of the cosmic microwave background (e.g., Komatsu et al. 2010) or luminosity distances of Type Ia supernovae (e.g., Hicken et al. 2009). The potential of cluster surveys as a cosmological probe has recently been demonstrated through the analysis of large X-ray and optically selected cluster samples spanning a wide range in redshift (e.g., Vikhlinin et al. 2009; Mantz et al. 2010; Rozo et al. 2010).

A powerful method for cluster detection and characterization is provided by the thermal Sunyaev-Zel'dovich (SZ) effect. The SZ effect is the process by which energy is transferred from the hot intra-cluster medium (ICM) of galaxy clusters to the cosmic microwave background (CMB) through inverse Compton scattering (Zel'dovich & Sunyaev 1969; Sunyaev & Zel'dovich 1970). The overall effect is to distort the thermal spectrum of the CMB. In the case of the present study at 148 GHz, the SZ distortion produces a roughly arcminute-scale temperature decrement along the line of sight to a galaxy cluster. The SZ distortion is proportional to the pressure of the ICM integrated along the line of sight, providing a unique probe of cluster physics. The integrated SZ flux therefore scales as the thermal energy content of the cluster, which is expected to scale with cluster mass for cluster gas hydrostatically supported by thermal pressure. The amplitude of the SZ distortion is approximately independent of the cluster redshift, in marked contrast to the observed cluster brightness in other wave bands. Therefore, the SZ effect is particularly suited for inventorying the distant universe. Galaxy cluster surveys are one of the few methods that probe the growth of structure and interpretation of survey yields has the potential to precisely constrain the equation of state of dark energy (e.g., Bartlett & Silk 1994; Holder et al. 2000; Haiman et al. 2001; Majumdar & Mohr 2004). For a full description of the SZ effect, historical perspectives, and applications to cosmology, see the review articles by Bernstein & Dodelson (1990), Birkinshaw (1991), Rephaeli (1995), Birkinshaw (1999), and Carlstrom et al. (2002).

The history of successful targeted observations of the SZ effect in previously known galaxy clusters goes back two decades. Pioneering measurements were made with the OVRO 40m telescope (Birkinshaw et al. 1991), the Ryle Telescope (Jones et al. 1993), the OVRO 5m telescope (Herbig et al. 1995; Myers et al. 1997), the OVRO/BIMA interferometers (Carlstrom et al. 1996), the bolometric SUZIE receiver on the Caltech Submillimeter Observatory (Holzapfel et al. 1997), and the Nobeyama Radio Observatory 45m telescope (Komatsu et al. 1999). Scientifically these original studies put special emphasis on deriving the Hubble parameter from angular diameter distances to clusters mea-

sured through a combination of SZ and X-ray data. In the last decade, these geometric measurements have been expanded to statistically significant samples of clusters (e.g., the OVRO/BIMA studies by Reese et al. 2002 and Bonamente et al. 2006) and serve as an independent check on estimates that rely on the conventional extragalactic distance ladder (e.g., Freedman et al. 2001; Riess et al. 2009). Beyond distance scale studies, targeted SZ work has focused on understanding the SZ correlation to other cluster observables, especially those which trace mass (e.g., Benson et al. 2004; Bonamente et al. 2008; McInnes et al. 2009; Marrone et al. 2009; Melin et al. 2010; Huang et al. 2010; Plagge et al. 2010; Culverhouse et al. 2010). The SZ/X-ray and SZ/optical lensing correlations provide the mass calibration necessary for understanding the cluster mass function through cosmic time. By measuring the redshift evolution of the cluster mass function, constraints can be put on the matter density field and dark energy. Thus proper mass calibration is essential for studying cosmology with clusters (e.g., Francis et al. 2005). Finally, targeted SZ observations are expanding our knowledge of the physics of the ICM by probing the cluster gas pressure at large radius (Mroczkowski et al. 2009; Plagge et al. 2010; Komatsu et al. 2010) as well as at high resolution (Komatsu et al. 2001; Mason et al. 2010).

The first blind detections of galaxy clusters through their Sunyaev-Zel'dovich effect were reported by Staniszewski et al. (2009) for the South Pole Telescope (SPT; Carlstrom et al. 2009). Three of the clusters from Staniszewski et al. (2009) were previously unknown. Hincks et al. (2009) reported on the cluster detections for the Atacama Cosmology Telescope (ACT; Fowler et al. 2007; Swetz et al. 2010). While the clusters from Hincks et al. (2009) were previously known, they were blindly detected in the survey data. SPT and ACT have been able to realize blind detections from cosmologically significant surveys because they combine three essential design features: arcminute resolution matched to the size of clusters, degree-scale fields of view for efficient surveying, and the unprecedented sensitivity of 1000-element bolometric detector arrays. In Vanderlinde et al. (2010), the SPT collaboration reported on twenty-one cluster candidates, twenty of which were optically confirmed (High et al. 2010). In a follow-up study, Andersson et al. (2010) presented the X-ray properties of the SPT sample and derived SZ/X-Ray correlations. Furthermore, Vanderlinde et al. (2010) obtained cosmological constraints from an SZ-selected sample of clusters.

In this work, the ACT collaboration reports on twenty-three clusters detected in a subset of the data taken during the 2008 observing season. This paper describes the detection and millimeter properties of the clusters. Companion papers describe the physical properties and observed purity of the cluster sample (Menanteau et al. 2010) as well as cosmological implications (Sehgal et al. 2010a). These papers and others cited above are part of a larger initial science release from ACT which also includes results on the CMB power spectrum and associated parameter constraints (Fowler et al. 2010; Das et al. 2010; Dunkley et al. 2010; Hajian et al. 2010) and on compact millimeter sources (Marriage et al.

³¹ Harvard-Smithsonian Center for Astrophysics, Harvard University, Cambridge, MA, USA 02138

³² Department of Astronomy, University of Massachusetts, Amherst, MA, USA 01003

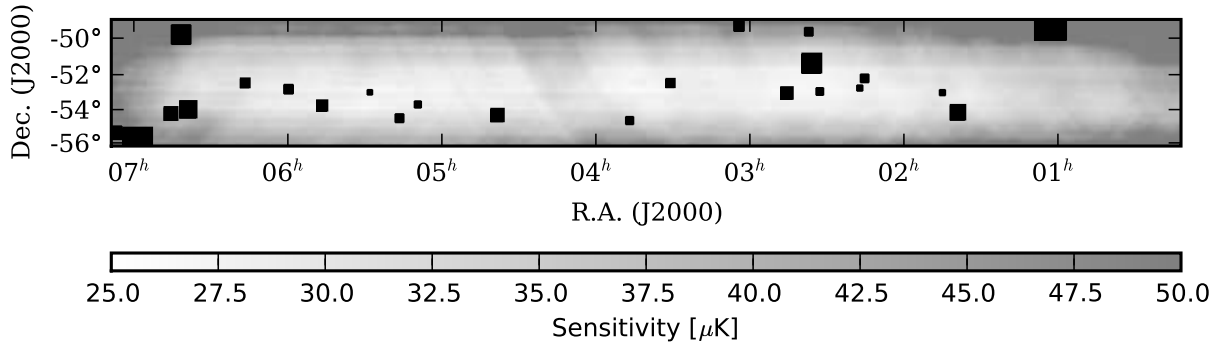


FIG. 1.— Sensitivity map with detections. The map shows the sensitivity over the subset of ACT 2008 148 GHz dataset considered for this study. The gray-scale encodes the noise rms in μK of a map match-filtered for a β -model ($\beta = 0.86$, $\theta_c = 1.00'$). The median noise in the map is $36\mu\text{K}$. Black boxes mark the location of the twenty-three optically confirmed clusters. The size of each box is proportional to the corresponding cluster decrement.

2010).

This paper is organized as follows. The data reduction and catalog construction are described in Section 2. The detections and their properties are discussed in Section 3. An estimate of purity and completeness of the sample is derived from simulations in Section 4. Finally, in Section 5, the SZ signal is compared to X-ray-derived mass for a high significance subset of the cluster sample.

2. FROM OBSERVATIONS TO CLUSTER DETECTION

The observations and methods to reduce the raw data to maps for this work are the same as used in the 2008 power spectrum study (Fowler et al. 2010) and extragalactic source study (Marriage et al. 2010). The primary difference between the source and cluster study lies in the compact signal profile used in the implementation of the matched filter-based detection. Therefore, we restrict our discussion here to a short summary of the observations and data reduction, and refer the reader to Fowler et al. (2010) and Marriage et al. (2010) for a more complete description. We describe in detail the particular implementation of the matched filter for clusters. For a description of the ACT receiver and instrumentation see Swetz et al. (2010).

2.1. Observations and Data Reduction

ACT is a six-meter telescope operating at 5200 m in the Atacama Desert of northern Chile. The site was chosen for its excellent atmospheric transparency and access to both southern and northern skies. The telescope has three 1024-element arrays of transition edge sensors operating at 148 GHz, 218 GHz, and 277 GHz. This study uses 148 GHz data from a 455-square-degree subregion of the 2008 southern survey. The subregion lies between right ascensions $00^{\text{h}}12^{\text{m}}$ and $07^{\text{h}}08^{\text{m}}$ and declinations $-56^{\circ}11'$ and $-49^{\circ}00'$. Figure 1 is a map of the sensitivity across the subregion along with the locations of the clusters reported in this study. The median rms of the map optimally filtered for detecting a β -model profile ($\beta = 0.86$, $\theta_c = 1.00'$) is $36\mu\text{K}$.

The data for this study were calibrated to the temperature of Uranus with a precision of 6%. The absolute positional uncertainty in the maps is established

at $3.5''$ by comparison of ACT radio source locations (Marriage et al. 2010) to cross-identified sources in the Australia Telescope 20 GHz Survey (Murphy et al. 2010). Note, however, that reported cluster locations have an additional uncertainty due to the effect of noise on the estimate of the cluster center. Considering the positional uncertainty for sources detected between signal-to-noise ratio (SNR) 5.5 and 10 reported in Marriage et al. (2010), we expect estimates of the ACT cluster center positions to scatter with an rms of roughly $10''$. Additional ambiguity in the cluster position arises in the case of an extended, non-spherical (e.g., disturbed) system. In such cases, the positional uncertainty can rise to arcminute scales.

With calibration and astrometry solved, the final step in the data reduction is map making. We iteratively solve for the maximum likelihood (ML) estimate of the map using a custom preconditioned conjugate gradient code (e.g., Press et al. 1992). Because ACT samples the sky along multiple scan directions (i.e., the data is cross-linked), we are able to produce an unbiased ML map of the microwave sky with a faithful representation of structure from degree to arcminute scales.

2.2. Filtering and Cluster Extraction

For cluster detection we use matched filters (Hahnelt & Tegmark 1996; Herranz et al. 2002; Melin et al. 2006). We model the sky temperature fluctuation at a point \mathbf{x} as

$$\delta T(\mathbf{x}) = \sum_i \delta T_{0,i} B_{\theta_c,i}(\mathbf{x} - \mathbf{x}_i) + \delta T_{\text{other}}(\mathbf{x}) \quad (1)$$

where $\delta T_{0,i}$ and $B_{\theta_c,i}$ are the amplitude and unit-normalized profile of the i^{th} cluster. In what follows we choose B_{θ_c} to be the isothermal β -model ($\beta = 0.86$) with core radius θ_c ranging from $0.25'$ to $4.0'$ and convolved with an isotropic ACT 148 GHz beam from Hincks et al. (2009). The profile is tapered to zero by multiplication with a cosine in the range 0.5 – $5.5\theta_c$. The choice of β is motivated by the best fit to an average SZ profile in Plagge et al. (2010) who found consistency between the β -model fit and the Generalized NFW profile fit to Y_X in

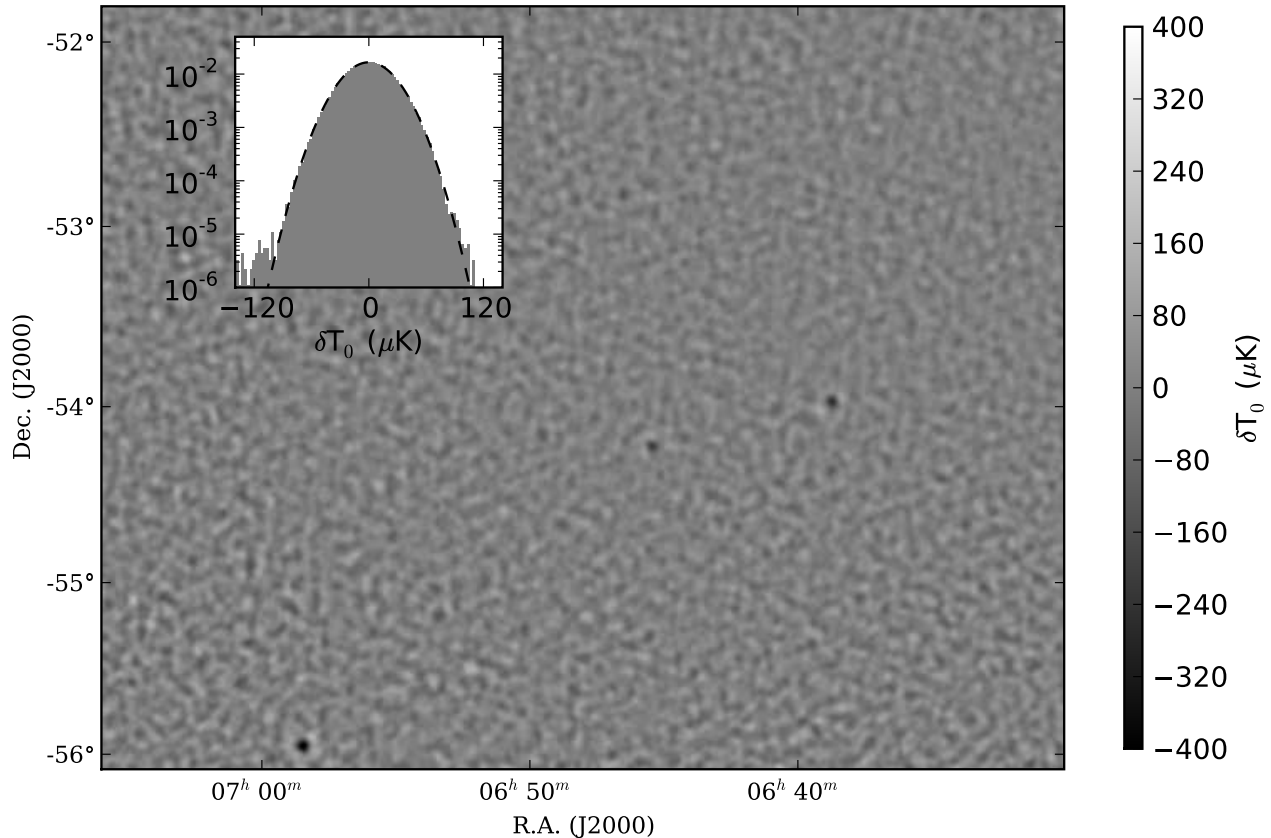


FIG. 2.— 148 GHz sub-map. The data have been weighted by a smooth function $\sqrt{N_{obs}/N_{obs,max}}$, where N_{obs} is the number of data per pixel. This weighting levels the amplitude of white noise across the map to that corresponding to the deepest data. The data is then match-filtered with a β -profile ($\theta_c = 1.0'$). The coverage becomes shallower toward the bottom-left of the map causing a visible increase in the rms. The inset shows the flux density distribution across the data weighted by the square-root of the number of data per pixel. The data distribution is shown as a gray histogram on which is plotted a dashed Gaussian distribution with standard deviation $24\mu\text{K}$. Sources were removed prior to filtering. Three clusters are recognizable from left to right: the Bullet Cluster (bottom-left), A3404 (middle), and AS0592 (middle-right).

Arnaud et al. (2009). The temperature field $\delta T_{\text{other}}(\mathbf{x})$ consists of noise modeled from difference maps, primordial CMB fluctuations with power spectrum from Nolta et al. (2009), as well as sources and undetectable (i.e., low mass) clusters. The spectral signature of the source and cluster contribution to $\delta T_{\text{other}}(\mathbf{x})$ is modeled from fits to ACT data in Fowler et al. (2010). See Marriage et al. (2010) for a full discussion of $\delta T_{\text{other}}(\mathbf{x})$.

Before filtering, bright ($\text{SNR} > 5$) sources are inpainted with sky temperature in the neighborhood of the source. Furthermore, the map is weighted by the inverse square root of the number of observations. This has the effect of flattening the white noise across the map. The map is filtered in the Fourier domain using a matched filter:

$$\delta T_{\text{filt}}(\mathbf{k}) = \frac{\tilde{B}_{\theta_c}^*(\mathbf{k}) |\tilde{\delta T}_{\text{other}}(\mathbf{k})|^{-2} \delta T(\mathbf{k})}{\int \tilde{B}_{\theta_c}^*(\mathbf{k}') |\tilde{\delta T}_{\text{other}}(\mathbf{k}')|^{-2} \tilde{B}_{\theta_c}(\mathbf{k}') d\mathbf{k}'} \quad (2)$$

where $\tilde{B}_{\theta_c}(\mathbf{k})$ and $\tilde{\delta T}_{\text{other}}(\mathbf{k})$ are the Fourier transforms

of B_{θ_c} and δT_{other} , respectively. The map is filtered using β -models with core radii from $0.25'$ to $4.0'$ in $0.25'$ steps. These core radii were chosen to span the range of angular scales characterizing massive clusters from low to high redshift. In a given map, the SNR of a detection is defined as the ratio of the extremum of the cluster decrement to the rms of the filtered map. The reported SNR for a given detection is the maximum SNR from the set of filtered maps. Figure 2 shows a subsection of the source-masked and filtered map containing three known clusters. Shown in an inset of this figure is the pixel flux distribution of the filtered map. The flux distribution suggests the filtered map is dominated by Gaussian noise.

The filter in Eq. 2 is normalized such that the central decrement in the filtered map is an estimate of the central decrement value in μK . It is this value, recovered from the filtered map, which we use as our decrement estimate. As discussed in Marriage et al. (2010), this estimate suffers from increased error and bias due to the

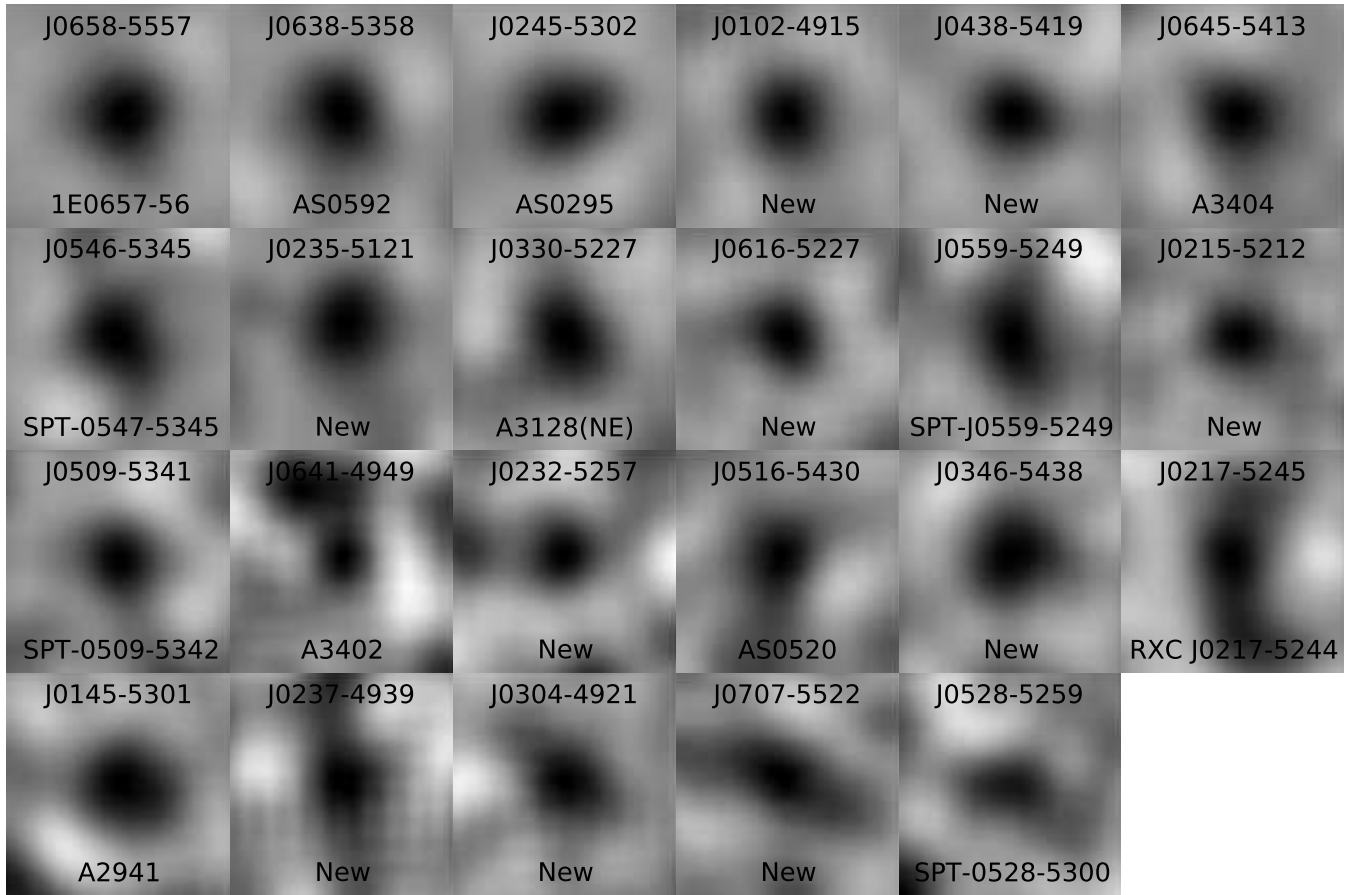


FIG. 3.— Temperature decrements at 148 GHz of twenty-three clusters. Each thumbnail is approximately $8'$ on a side and is excised from the source-removed, filtered map. The grayscale of each thumbnail is symmetric about zero with a range set to the depth of the decrement. The ordering of the clusters is according to decreasing SNR from left to right and top to bottom. The structure northeast of ACT-CL J0641-4949 may be part of the cluster or may be contamination: the decrement of this nearby cluster may be noise boosted. ACT designations are at the top of each thumbnail and alternate names at the bottom, denoted “New” if newly discovered by ACT.

$0.5'$ pixel size of the ACT maps. In order to mitigate these errors, the pixel size of sub-maps around each detection is decreased by Fourier transforming the map and adding extra zeros to the boundary of the Fourier transform. The inverse of this zero-padded transform is then the original submap with smaller pixels. For this study, the pixel size is changed to $0.0625'$ which reduces the errors associated with the discrete approximation of Eq. 2 to less than 1%. The errors we quote for the map-derived decrements are simply the decrement amplitude divided by the SNR.

3. CLUSTER DETECTIONS AND PROPERTIES

Table 1 lists clusters detected by ACT. All detections in the table have been confirmed through optical follow-up imaging of a larger catalog of all SZ candidates from the ACT data (Menanteau et al. 2010). The table is divided into two groups of candidates: candidates detected at $\text{SNR} > 6$ and candidates detected at lesser significance. The optical follow-up showed that for candidates detected at $\text{SNR} > 6$, the larger catalog of all SZ candidates is 100% pure (See also Section 4.). Of the nine detections at $\text{SNR} > 6$, three are newly discovered systems. Among the fourteen candidates confirmed at lower SNR, seven are new detections. Thumbnails of the cluster decrements are shown in Figure 3.

The multifrequency properties of the clusters covered in this work are discussed at length in Hincks et al. (2009) and Menanteau et al. (2010). Paraphrasing these studies, X-ray luminosities were computed from Chandra and XMM observations where available and supplemented by ROSAT All Sky Survey for the remaining clusters. These luminosities suggest that the full sample is composed of high mass clusters with a characteristic mass of $M_{500c} \sim 6 \times 10^{14} M_{\odot}$, where M_{500c} is defined as the mass of the cluster at five hundred times the critical density of the universe at the cluster redshift. The sample has a median redshift of 0.44. All but one of the clusters at $z > 0.35$ in the sample were discovered via the SZ.

Of the new ACT clusters, the most notable is ACT-CL J0102-4915. This cluster has a decrement amplitude ($\delta T' = -1046 \pm 116 \mu K$) comparable to that of the Bullet Cluster ($\delta T' = -734 \pm 64 \mu K$) as well as a smaller angular core radius, consistent with its higher redshift ($z_{\text{photo}} = 0.75$). The X-ray luminosity (0.1–2.4 keV) derived from ROSAT observations is $18.39 \pm 6.49 \times 10^{44} \text{ erg s}^{-1}$ which is also comparable to that of the Bullet as well as the other massive clusters in our sample (Menanteau et al. 2010). The cluster richness is also consistent with that of a massive cluster ($N_{\text{gal}} \approx 50$). The strength of this decrement may result from merger activity, elongation

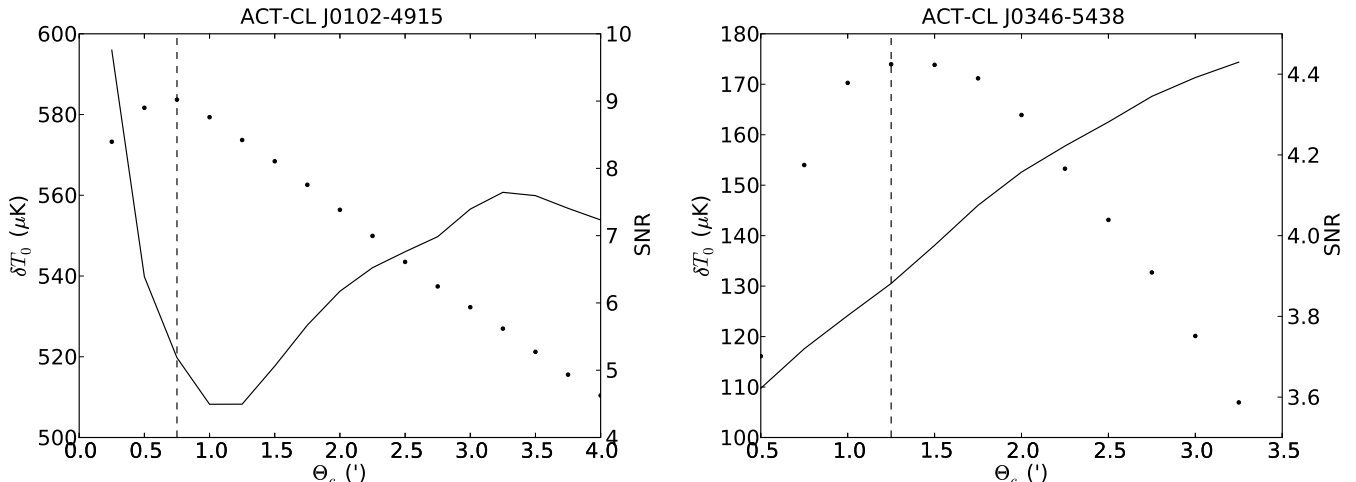


FIG. 4.— Decrement amplitude and SNR versus the filter core radius for two newly discovered clusters. The solid curve corresponds to the decrement while the dotted curve corresponds to the SNR. A vertical dashed line marks the maximum SNR identified by the extraction algorithm.

along the line of sight, or other decrement-enhancing effects. Planned spectroscopic and IR follow-up observations will determine the true nature of the decrement.

Table 1 contains estimates of the cluster decrement amplitudes δT_0 based upon the matched filter described in Section 2.2. Also listed is the core radius θ_c corresponding to the filter that exhibits the largest SNR for each cluster. Figure 4 shows the temperature decrement and SNR of two newly discovered clusters plotted as a function of filter scale (i.e., the core radius). For some of the clusters, such as ACT-CL J0346-5438 shown in the figure, the SNR is a relatively broad function of core radius. The corresponding uncertainty in the size of the cluster results from the blending of the cluster decrement with the background (e.g., CMB). This confusion for single-frequency data was observed by Melin et al. (2006) as well as Vanderlinde et al. (2010). For clusters with a more compact and pronounced core, like ACT-CL J0102-4915, the cluster-background confusion is smaller and so the optimal filter scale is easier to determine from the data. Confusion with the background inflates θ_c while contamination by detector white noise causes a cluster to appear more compact than it actually is. The latter effect can be explained by the fact that most of the power in the white noise field is at the smallest scales. Simulations (See Section 4.) show contamination for clusters detected outside the range $\theta_c = 0.75' - 1.75'$. For this reason, θ_c estimates reported below $0.75'$ or above $1.75'$ are suspect. Incorporation of ACT’s multiple frequencies will help distinguish clusters from background. Additional years of data will help reduce the fraction of white-noise-boostered detections.

The δT_0 recovered from the filter is the amplitude of the cluster decrement in the ACT map. As such, it is the amplitude of the intrinsic cluster profile convolved with the ACT beam. In Table 1 we also include an estimate of the decrement $\delta T'_0 = \delta T_0 C^{-1}(\theta_c)$ where we have corrected the raw δT_0 by the smearing effect of the beam on the height of the corresponding β -profile. This correction for a β -profile with $\theta_c = 1'$ is 1.67. The correction is larger for smaller core radii. To estimate the uncer-

tainty in the recovered $\delta T'_0$, the cluster extraction algorithm was run on a simulation with realistic ACT noise, CMB and clusters with symmetric β -model profiles. The more realistic simulations of Sehgal et al. (2010b) were not used as they were not provided an estimate of the decrement amplitude. As the β -model profiles in this simulation are matched to our filters, the error estimate from these simulations should be taken as a lower limit. With those caveats, the mean error on $\delta T'_0$ from the simulations is 20% greater than the statistical error inferred from the SNR (i.e., systematic errors are 40% of the total error budget). This modest increase in the error budget was accompanied by a large scatter in recovered scale ($\sim 30\%$ with respect to the input scale value) with a non-Gaussian tail towards larger recovered radii. This implies that while the physical scale of the cluster may be confused with the background the amplitude of the peak is relatively immune to this confusion. When the cluster extraction algorithm was run on the β -model simulations with prior knowledge of the scale, the resulting scatter in recovered $\delta T'_0$ values was consistent with the statistical error inferred from the SNR. Thus we infer that, in the ideal case of β -model cluster profiles, uncertainty in scale adds 20% scatter to our uncertainty in $\delta T'_0$. For more realistic cluster profiles (e.g., asymmetric), this scatter should be larger.

Because the cluster counts are a falling function of mass (and therefore of decrement amplitude), clusters detected at low significance are more likely to be lower mass systems with a noise-boostered decrement than a higher mass system with a noise-suppressed decrement. In particular, members of the lower significance ($\text{SNR} < 6$) fraction of the ACT detections are likely to have their $\delta T'_0$ overestimated due to noise-boostered. In this work, no correction has been made for this bias. An additional bias arises from optimizing the detection significance over the two celestial coordinates and θ_c . Vanderlinde et al. (2010) show that this latter bias, when referred to SNR, can be shown to be $\sqrt{\text{SNR}^2 - 3}$. In the case of $\text{SNR} = 4$, therefore, the optimization over location and core radius increases the raw decrement estimate by 10% on average.

Decrement measurements at 150 GHz have been published for a number of the known clusters in the current ACT sample. Halverson et al. (2008) using the APEX telescope reported a decrement for the Bullet Cluster $-771 \pm 71 \mu\text{K}$ while Plagge et al. (2010) using the South Pole Telescope reported $-932 \pm 43 \mu\text{K}$. Plagge et al. (2010) also found decrements for AS 0520 ($-217 \mu\text{K}$), A 3404 ($-472 \mu\text{K}$), AS 0592 ($-529 \mu\text{K}$), and RXC J0217.2-5244 ($-217 \mu\text{K}$) all of which are in reasonable agreement with the $\delta T'_0$ values in Table 1. The central values of the SPT estimates are, however, systematically more negative than the central values reported in Table 1.

Table 1 also contains the central Compton y parameter y'_0 which is related to the central decrement $\delta T'_0$ by :

$$\frac{\delta T'_0}{T_{CMB}} = y'_0 \left(x \frac{e^x + 1}{e^x - 1} - 4 \right) (1 + \delta_{SZE}(x, T_e)). \quad (3)$$

In this equation $x = h\nu/k_B T_{CMB}$ and T_e is the temperature of the electron gas. In this equation, we have omitted the $\sim 10\%$ contribution of the kinetic Sunyaev-Zel'dovich (kSZ) effect which arises due to the peculiar velocity of the cluster (Sunyaev & Zel'dovich 1970). Because we do not know the bulk velocity of the clusters, we do not account for the contribution of the kinetic effect which adds to the uncertainty in the derived y parameter. The y parameter itself is the product of the optical depth through the cluster and $k_B T_e/m_e c^2$ where m_e is the electron mass:

$$y'_0 = \frac{k_B T_e}{m_e c^2} \int n_e \sigma_T dl \quad (4)$$

where σ_T is the Thomson cross section and isothermality of the cluster is assumed. The relativistic correction $\delta_{SZE}(x, T_e)$ at 148 GHz varies from -0.03 to -0.10 for the ACT sample, corresponding to cluster temperatures in the range 5–15 keV (Nozawa et al. 2006). We have used X-ray temperatures tabulated in Menanteau et al. (2010) as input to the relativistic correction for a subset of the clusters. For clusters without an X-ray temperature, we use a correction of -0.05 which roughly corresponds to a temperature of 7.5 keV, characteristic of our sample.

For all but one case, there is no obvious correlation of the cluster decrements with strong sources. The one exception is Abell S0295. Approximately $4'$ north-east of the cluster is ACT-S J024539-525756 (Marriage et al. 2010) with a 148 GHz flux density of 18.4 mJy (SNR=7.6). The source is also identified at 0.84 GHz in the Sydney University Molonglo Sky Survey (SUMSS) catalog (Mauch et al. 2003). Therefore the source flux density is most likely dominated by synchrotron emission. From simple geometric arguments, there is approximately a 10% chance that one of the the ACT sources would randomly fall within $4'$ of one of the twenty-three clusters, so the source-cluster proximity may be a projection effect. Furthermore, the source's large angular displacement from the cluster implies that it is unlikely a lensed background galaxy. Finally, note that this source does not appear near Abell S0295 in Figure 3 because the source was removed from the data prior to filtering.

There are slight differences between the cluster properties as presented in Table 1 and in Menanteau et al. (2010). The SNR and, to a lesser degree, position differ

due primarily to two facts. First, the data reduction (i.e., the map) used for Menanteau et al. (2010) was a preliminary version of that used for this work. The map used for this work corresponds to that used in Fowler et al. (2010) and Marriage et al. (2010). Second, the signal and noise terms used in the matched filter for the candidate selection in Menanteau et al. (2010) are different from those used in this study. These differences in analysis arose from the need to execute the optical follow-up before the ACT pipeline and cluster extraction algorithm were fully mature. The differences in SNR generally correspond to approximately 1σ fluctuations between the reductions.

4. SIMULATED PURITY AND COMPLETENESS

In order to assess the ratio of true detections to total detections (purity) and the fraction of clusters recovered (completeness), we run our filtering and extraction algorithm on simulations of the ACT data. The simulations were constructed using the millimeter signal (SZ, CMB, etc.) from Sehgal et al. (2010b) and noise from ACT difference maps. In order to avoid confusion due to source-SZ correlations included in Sehgal et al. (2010b), the source component of those simulations was not included. The undetected/unmasked sources in the data contribute a small fraction of the rms of the filtered map which is dominated by white detector and photon shot noise (Marriage et al. 2010).

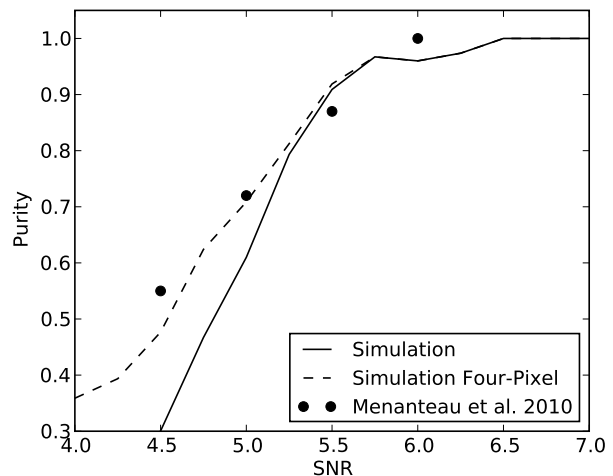


FIG. 5.— Simulated purity. Purity is defined as fraction of true detections in the sample. The four-pixel candidate selection, which was used to produce the sample in Menanteau et al. (2010), requires cluster candidates to have at least four pixels with $\text{SNR} > 4.0$. The dashed line gives the simulated purity associated with the four-pixel selection function. The solid line is the purity function corresponding to a selection function based on the single highest SNR cluster pixel. As expected the four-pixel purity of the simulated sample is in reasonable agreement with that derived from optical follow-up of candidates from the data Menanteau et al. (2010). The sample is essentially pure at $\text{SNR} > 6$.

Although it is expected that, from a noise power perspective, omitting the sources in this study will not significantly impact the analysis, there remains concern that millimeter sources may be correlated with clusters, either as cluster members or as lensed backgrounds. Studying 573 nearby clusters with 1.4 GHz data from the NRAO

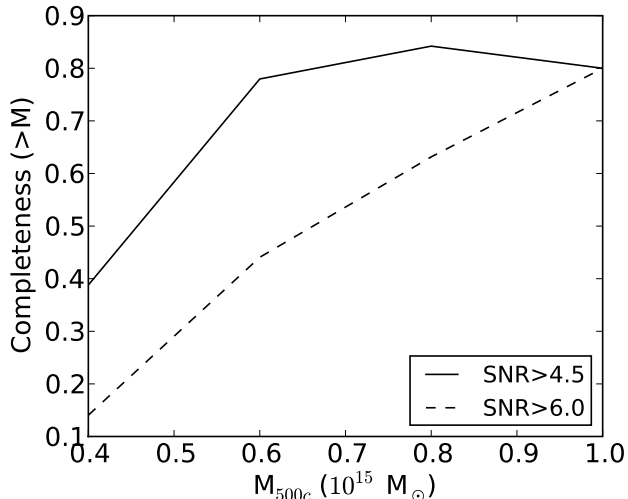


FIG. 6.— Cumulative completeness of the simulated sample. At $M_{500c} > 6 \times 10^{14} M_{\odot}$ the approximation to the total sample (SNR > 4.5) is $\sim 80\%$ complete. The completeness degrades at the edges of the map: taking the cleanest 230 sq-deg from Fowler et al. (2010), the completeness rises to 90%.

VLA Sky Survey, Lin & Mohr (2007) found that the fraction of BCGs being radio-loud is higher compared to that of cluster galaxies of similar luminosity. Extrapolating in frequency and redshift, this study concluded that roughly 10% of clusters may have 150 GHz decrements “filled in” by synchrotron emission from resident AGN. Marriage et al. (2010) included a cross-comparison of the 150 GHz bright source population detected by ACT and the 23 REFLEX X-ray clusters (Böhringer et al. 2004) which fall within the survey area. The study cross-identified three clusters with 150 GHz sources. These three clusters were all at redshifts below $z = 0.06$ in contrast to the higher redshift sample of this work. Lensed background dusty star-forming galaxies may also contaminate the SZ signal. Wilson et al. (2008) found a bright, lensed, dusty source at 1.1 mm behind the Bullet Cluster. Vieira et al. (2010) found that the lensed dusty population were characterized by maximum 150 GHz flux densities below 5 mJy range. This finding is consistent with the Wilson et al. (2008) bright Bullet Cluster lensed source flux of 15.9 mJy at 1.1 mm (~ 4 mJy at 150 GHz assuming a spectral index of 2). Filtered at characteristic scale ($.75'$) of this work, such sources would produce a peak brightness of $10 \mu\text{K}$. As the decrements in this work measure of order $100 \mu\text{K}$, contributions from dusty sources may affect the purity and completeness of faint end of the sample, but the bright end (SNR > 6) should be relatively immune to detection problems due to dusty sources.

In order to build simulated catalogs to compare to that from the data, we run the filtering and detection pipeline described in Section 2.2 on each of six simulations extracted from the Sehgal et al. (2010b) sky. We identify decrements with clusters from the simulated catalog with $M_{500c} > 2 \times 10^{14} M_{\odot}$ and at redshifts $z > 0.1$. The identification radius is $3'$. This radius was chosen by studying significant decrements detected in the simulations and their offset from the position reported in the simulated catalog. By coincidence, this is also ap-

proximately the size of the optical fields of view used in the Menanteau et al. (2010) follow-up work. In nearly all cases, the arcminute scale displacements resulted from extended non-spherical, often double peaked, clusters. In these cases it was easier for noise fluctuations to move the detection position away from the minimum of the cluster potential as reported in the catalogs from Sehgal et al. (2010b).

Figure 5 shows the purity as derived from the simulations. In order to reproduce the original selection function from Menanteau et al. (2010) we require that a cluster candidate have four conjoined map pixels with SNR > 4.0. This requirement is intended to boost the purity of the sample with respect to a sample drawn with the requirement that only a single pixel have a high SNR. Figure 5 shows the purity versus SNR for both of these selection effects. As expected, the four-pixel requirement increases the purity as determined by the simulations. Furthermore the four-pixel purity agrees reasonably well with the purity measured in Menanteau et al. (2010). The simulations imply that the purity of the sample with SNR > 6 is 95%, consistent with the finding that all these clusters have optical counterparts. Furthermore, both the four-pixel and single-pixel selection process yield the same purity for the high SNR sample. Below SNR = 6, simulations show that the four-pixel purity falls off in a manner consistent with the purity determined from the optical follow-up. The single-pixel purity falls significantly faster with decreasing SNR compared to that of the four-pixel or optically-measured purity. We therefore choose the four-pixel selection function to evaluate the completeness of the sample below.

It is straightforward to simulate the cumulative completeness as a function of cluster mass for the pure population at SNR > 6. As shown in Figure 6 with the dashed curve, we count the simulated clusters above a given mass and detected at SNR > 6. We then divide the number of detected clusters by the total number of clusters in the same mass range. The resulting cumulative completeness shows that the high SNR sample is approximately $\sim 45\%$ complete for $M_{500c} > 6 \times 10^{14} M_{\odot}$ and rises to 80% complete for $M_{500c} > 1.0 \times 10^{15} M_{\odot}$. One reason for incompleteness among the high mass population is that clusters at $z < 0.3$ are characterized by larger angular scales than their high-redshift counterparts and start blending with the fluctuations in the cosmic microwave background. Dividing the simulated sample in redshift bins of $\delta z = 0.2$ bins between $z = 0.1$ and $z = 1.1$, the completeness of this sample, in the mass range $M_{500c} > 6 \times 10^{14} M_{\odot}$, increased smoothly from 30% in the lowest redshift ($z = 0.1-0.3$) bin to 70% complete in the highest bin ($z = 0.9-1.1$).

It is not so straightforward to reproduce the cumulative completeness function for the entire sample presented in Menanteau et al. (2010) which is based on a previous reduction of the data. As shown in Figure 13 of Menanteau et al. (2010), the follow-up observations were completed for a preliminary candidate list down to SNR = 4.2. Below SNR = 4.8, the follow-up was performed for a decreasing fraction of candidates such that, by SNR = 4.2, the fraction of the total candidates followed up was 50%. In order to approximately simulate the smoothly declining selection function of the follow-up for candidates in the range SNR = 4.2-4.8, we simply introduce a hard cut at SNR = 4.5 where the sampling

goes from 100% to 0%.

With this prescription for modeling the entire sample, the simulations suggest that $\sim 80\%$ of all clusters with $M_{500c} > 6 \times 10^{14} M_{\odot}$ are detected. Figure 6 shows the full cumulative completeness function with a solid curve. Unlike in the case of the high SNR sample discussed above, the simulations suggest that completeness of the full sample in the range $M_{500c} > 6 \times 10^{14} M_{\odot}$ is not a strong function of redshift ($z = 0.1\text{--}1.1$). Another important reason for the incompleteness is that a fraction of massive clusters are disturbed, showing elongated structure in the plane of the sky, and thus are not well matched to our β -model filter. Conversely, the simulations suggest our sample likely includes high-redshift relaxed, spherical clusters of lower mass (e.g., $4 \times 10^{14} M_{\odot}$). Another feature of the data which drives the overall completeness down is the high level of noise towards the edge of the map. If the region under consideration is restricted to the central 230 square degrees used for the power spectrum study in Fowler et al. (2010), then the completeness estimate for clusters with $M_{500c} > 6 \times 10^{14} M_{\odot}$ increases to $\sim 90\%$.

5. SZ-MASS CORRELATION

In this section, we perform a largely illustrative, preliminary study of the correlation of the SZ signal with mass for the more significant ($\text{SNR} > 5$) half of the SZ detections. For the SZ signal we use the central y'_0 as described in Section 3 and listed in Table 1. For the total mass, we derive M_{500c} using X-ray luminosities from Menanteau et al. (2010) and the $L_x - M$ relation from Vikhlinin et al. (2009). For all clusters but Abell 3128(NE), the X-ray luminosities were derived from the ROSAT All Sky Survey. For Abell 3128(NE), the available higher resolution Chandra results from Menanteau et al. (2010) were used to help separate the flux from the more massive background cluster from the less massive cluster at low redshift (Werner et al. 2007). An additional scale factor of ~ 1.6 was needed to convert the luminosities from the 0.1-2.4 keV band in Menanteau et al. (2010) to the 0.5-2.0 keV band required by the correlation in Vikhlinin et al. (2009). The resulting M_{500c} estimates are shown in Table 2. The error given for M_{500c} only includes statistical error propagated from error on L_x . Additional scatter about this relation was measured to be 48% (Vikhlinin et al. 2009). due to evolution and non-trivial processes in the ICM as well as Ongoing optical and X-ray follow-up of the ACT cluster sample will improve these mass estimates in the near future.

For self-similar evolution, the central y'_0 is expected to scale as $ME^2(z)$ where $E^2(z) = \Omega_M(1+z)^3 + \Omega_{\Lambda}$ for a flat Λ CDM universe. The conventional argument behind this scaling is given in Appendix A. Anticipating such a scaling, in Figure 7 we plot y'_0 values scaled by $E^{-2}(z)$ against their corresponding M_{500c} estimates. Values used for Ω_M and Ω_{Λ} are 0.26 and 0.74, respectively (Komatsu et al. 2010). The errors plotted for y'_0 are purely statistical. As discussed in Section 3, systematic errors, primarily due to uncertainty in the core radius, would increase the errors on y'_0 by at least 20%. Because of systematic uncertainties associated with the estimators for y'_0 and M_{500c} no attempt has been made to fit scaling relations to these data. Given this pre-

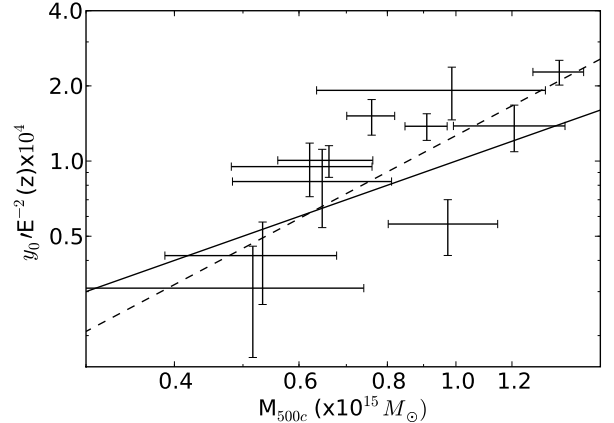


FIG. 7.— SZ-Mass Correlation. Estimated Compton y parameter estimates (Table 1) are plotted, scaled for self-similar evolution, against X-ray luminosity-derived mass estimates (Table 2) for the more significant half ($\text{SNR} > 5$) of the cluster sample. The line plotted is the self-similar model $y'_0 \propto ME^2(z)$ (See Appendix A.). The model, which is not fit to the data, agrees reasonably well with the ACT data. For comparison, the dashed line shows a simulation-motivated model with logarithmic slope 3/2 (Motl et al. 2005).

caution, however, the data appear consistent with the self-similar model plotted as a solid line in the figure. An additional dashed line with $y'_0 \propto M^{3/2}E^2(z)$ approximates the $y_0 - M$ relation from numerical simulations including star formation and supernova feedback from Motl et al. (2005). The data also appear consistent with this model.

The SZ-Mass relation presented here is for illustrative purposes using central y parameter estimates and a mass proxy that are available now for all clusters but which have a large scatter. The SZ signal estimate will be improved in future analyses using additional ACT bands as well as additional information on cluster gas and temperature profiles from the X-ray (e.g., Andersson et al. 2010). The precise relationship between the SZ signal and mass needs to be determined from more precise mass proxies such as X-ray temperature, galaxy velocity dispersion, and weak lensing. This work is in progress and will be reported in future publications.

6. CONCLUSION

ACT has identified the SZ signatures of twenty-three optically-confirmed galaxy clusters at a frequency of 148 GHz in data taken during the 2008 observing season. Of these clusters, ten are new discoveries. Together, ACT and SPT have reported twenty-five newly discovered systems. The Planck Satellite will soon add its complementary detections to the growing sample of SZ cluster discoveries. Due to the unique nature of the SZ effect, the sample is biased towards high-mass clusters at high redshifts. As such the sample complements current X-ray and optically-selected catalogues. Among the clusters discovered by ACT, ACT-CL J0102-4915 stands out as a high redshift cluster having an SZ temperature decrement comparable to that of the most massive known clusters. Purity estimates from simulations of the cluster extraction agree with the sample purity derived from optical follow-up in Menanteau et al. (2010). The simulations also estimate completeness of the sample at roughly 80% for $M_{500c} > 6 \times 10^{14} M_{\odot}$. Over the same mass range, the completeness increases to greater than

90% if only the lowest noise half of the survey area is considered. A comparison of the clusters' central Compton y parameters with X-ray luminosity-derived masses is in agreement with both self-similar scaling as well as scalings based on simulations which include star formation and supernova feedback.

Future work with the SZ effect from galaxy clusters will include ACT data from multiple seasons and multiple millimeter bands. In addition to the southern survey described in this work, ACT is also surveying the celestial equator to complement extant and future multifrequency cluster work in this highly accessible strip of sky.

The ACT project was proposed in 2000 and funded by the U.S. National Science Foundation on January 1, 2004. Many have contributed to the project since its inception. We especially wish to thank Asad Aboobaker, Christine Allen, Dominic Benford, Paul Bode, Kristen Burgess, Angelica de Oliveira-Costa, Sean Frazier, Nick Hand, Peter Hargrave, Norm Jarosik, Amber Miller, Carl Reintsema, Felipe Rojas, Uros Seljak, Martin Spergel, Johannes Staguhn, Carl Stahle, Max Tegmark, Masao Uehara, Katerina Visnjic, and Ed Wishnow. It is a pleasure to acknowledge Bob Margolis, ACT's project manager. Reed Plimpton and David Jacobson worked at the telescope during the 2008 season. Naoki Itoh and Satoshi Nozawa provided code for calculating relativistic corrections to the SZ. ACT operates in the Parque Astronómico Atacama in northern Chile under the auspices of Programa de Astronomia, a program of the Comisión Nacional de Investigación Científica y Tecnológica (CONICYT).

This work was supported by the U.S. National Science

Foundation through awards AST-0408698 for the ACT project, and PHY-0355328, AST-0707731 and PIRE-0507768. Funding was also provided by Princeton University and the University of Pennsylvania. The PIRE program made possible exchanges between Chile, South Africa, Spain and the US that enabled this research program. Computations were performed on the GPC supercomputer at the SciNet HPC Consortium. SciNet is funded by: the Canada Foundation for Innovation under the auspices of Compute Canada; the Government of Ontario; Ontario Research Fund – Research Excellence; and the University of Toronto.

TM was supported through NASA grant NNX08AH30G. JBJ was supported by the FONDECYT grant 3085031. ADH received additional support from a Natural Science and Engineering Research Council of Canada (NSERC) PGS-D scholarship. AK and BP were partially supported through NSF AST-0546035 and AST-0606975, respectively, for work on ACT. HQ and LI acknowledge partial support from FONDAP Centro de Astrofísica. NS is supported by the U.S. Department of Energy contract to SLAC no. DE-AC3-76SF00515. RD was supported by CONICYT, MECESUP, and Fundación Andes. RH was supported by the Rhodes Trust. ES acknowledges support by NSF Physics Frontier Center grant PHY-0114422 to the Kavli Institute of Cosmological Physics. YTL acknowledges support from the World Premier International Research Center Initiative, MEXT, Japan. The ACT data will be made public through LAMBDA (<http://lambda.gsfc.nasa.gov/>) and the ACT website (<http://www.physics.princeton.edu/act/>).

REFERENCES

- Andersson, K., et al. 2010, arXiv:1006.3068
- Arnaud, M., Pratt, G. W., Piffaretti, R., Boehringer, H., Croston, J. H., & Pointecouteau, E. 2009, arXiv:0910.1234
- Bartlett, J. G., & Silk, J. 1994, ApJ, 423, 12
- Benson, B. A., Church, S. E., Ade, P. A. R., Bock, J. J., Ganga, K. M., Henson, C. N., & Thompson, K. L. 2004, ApJ, 617, 829
- Bernstein, J., & Dodelson, S. 1990, Phys. Rev. D, 41, 354
- Birkinshaw, M. 1991, in Physical Cosmology, ed. A. Blanchard, L. Celnikier, M. Lachieze-Rey, & J. Tran Thanh Van, 177–187
- Birkinshaw, M. 1999, Phys. Rep., 310, 97
- Birkinshaw, M., Hughes, J. P., & Arnaud, K. A. 1991, ApJ, 379, 466
- Bonamente, M., Joy, M., LaRoque, S. J., Carlstrom, J. E., Nagai, D., & Marrone, D. P. 2008, ApJ, 675, 106
- Bonamente, M., Joy, M. K., LaRoque, S. J., Carlstrom, J. E., Reese, E. D., & Dawson, K. S. 2006, ApJ, 647, 25
- Böhringer, H., et al. 2004, A&A, 425, 367
- Bryan, G. L., & Norman, M. L. 1998, ApJ, 495, 80
- Carlstrom, J. E., Holder, G. P., & Reese, E. D. 2002, ARA&A, 40, 643
- Carlstrom, J. E., Joy, M., & Grego, L. 1996, ApJ, 456, L75+
- Carlstrom, J. E., et al. 2001, PASP, 123, 568
- Culverhouse, T. L., et al. 2010, arXiv:1007.2853
- Das, S., et al. 2010, arXiv:1009.0847
- Dunkley, J., et al. 2010, arXiv:1009.0866
- Fowler, J. W., et al. 2007, Appl. Opt., 46, 3444
- Fowler, J. W., et al. 2010, arXiv:1001.2934
- Francis, M. R., Bean, R., & Kosowsky, A. 2005, JCAP, 12, 1
- Freedman, W. L., et al. 2001, ApJ, 553, 47
- Haehnelt, M. G., & Tegmark, M. 1996, MNRAS, 279, 545
- Haiman, Z., Mohr, J. J., & Holder, G. P. 2001, ApJ, 553, 545
- Hajian, A., et al. 2010, arXiv:1009.0777
- Halverson, N. W., et al. 2008, arXiv:0807.4208
- Foundation through awards AST-0408698 for the ACT project, and PHY-0355328, AST-0707731 and PIRE-0507768. Funding was also provided by Princeton University and the University of Pennsylvania. The PIRE program made possible exchanges between Chile, South Africa, Spain and the US that enabled this research program. Computations were performed on the GPC supercomputer at the SciNet HPC Consortium. SciNet is funded by: the Canada Foundation for Innovation under the auspices of Compute Canada; the Government of Ontario; Ontario Research Fund – Research Excellence; and the University of Toronto.
- TM was supported through NASA grant NNX08AH30G. JBJ was supported by the FONDECYT grant 3085031. ADH received additional support from a Natural Science and Engineering Research Council of Canada (NSERC) PGS-D scholarship. AK and BP were partially supported through NSF AST-0546035 and AST-0606975, respectively, for work on ACT. HQ and LI acknowledge partial support from FONDAP Centro de Astrofísica. NS is supported by the U.S. Department of Energy contract to SLAC no. DE-AC3-76SF00515. RD was supported by CONICYT, MECESUP, and Fundación Andes. RH was supported by the Rhodes Trust. ES acknowledges support by NSF Physics Frontier Center grant PHY-0114422 to the Kavli Institute of Cosmological Physics. YTL acknowledges support from the World Premier International Research Center Initiative, MEXT, Japan. The ACT data will be made public through LAMBDA (<http://lambda.gsfc.nasa.gov/>) and the ACT website (<http://www.physics.princeton.edu/act/>).
- Herranz, D., Sanz, J. L., Barreiro, R. B., Hobson, M., Martinez-Gonzalez, E., & Diego, J. M. 2002, in Presented at the Society of Photo-Optical Instrumentation Engineers (SPIE) Conference, Vol. 4847, Society of Photo-Optical Instrumentation Engineers (SPIE) Conference Series, ed. J.-L. Starck & F. D. Murtagh, 50–61
- Hicken, M., Wood-Vasey, W. M., Blondin, S., Challis, P., Jha, S., Kelly, P. L., Rest, A., & Kirshner, R. P. 2009, ApJ, 700, 1097
- High, F. W., et al. 2010, arXiv:1003.0005
- Hincks, A. D., et al. 2009, arXiv:0907.0461
- Holder, G. P., Mohr, J. J., Carlstrom, J. E., Evrard, A. E., & Leitch, E. M. 2000, ApJ, 544, 629
- Holzappel, W. L., et al. 1997, ApJ, 480, 449
- Huang, C., et al. 2010, ApJ, 716, 758
- Jones, M., et al. 1993, Nature, 365, 320
- Komatsu, E., Kitayama, T., Suto, Y., Hattori, M., Kawabe, R., Matsuo, H., Schindler, S., & Yoshikawa, K. 1999, ApJ, 516, L1
- Komatsu, E., et al. 2001, PASJ, 53, 57
- . 2010, arXiv:1001.4538
- Lin, Y., & Mohr, J. J. 2007, ApJS, 170, 71
- Majumdar, S., & Mohr, J. J. 2004, ApJ, 613, 41
- Mantz, A., Allen, S. W., Rapetti, D., & Ebeling, H. 2010, MNRAS, 406, 1759
- Marriage, T. A., et al. 2010, arXiv:1007.5256
- Marrone, D. P., et al. 2009, ApJ, 701, L114
- Mason, B. S., et al. 2010, ApJ, 716, 739
- Mauch, T., Murphy, T., Buttery, H. J., Curran, J., Hunstead, R. W., Piestrzynski, B., Robertson, J. G., & Sadler, E. M. 2003, MNRAS, 342, 1117
- McInnes, R. N., Menanteau, F., Heavens, A. F., Hughes, J. P., Jimenez, R., Massey, R., Simon, P., & Taylor, A. N. 2009, arXiv:0903.4410

- Melin, J., Bartlett, J. G., & Delabrouille, J. 2006, *A&A*, 459, 341
- Melin, J., Bartlett, J. G., Delabrouille, J., Arnaud, M., Piffaretti, R., & Pratt, G. W. 2010, *A&A*, 525, A139
- Menanteau, F., et al. 2010, arXiv:1006.5126
- Motl, P. M., Hallman, E. J., Burns, J. O., & Norman, M. L. 2005, *ApJ*, 623, L63
- Mroczkowski, T., et al. 2009, *ApJ*, 694, 1034
- Murphy, T., et al. 2010, *MNRAS*, 402, 2403
- Myers, S. T., Baker, J. E., Readhead, A. C. S., Leitch, E. M., & Herbig, T. 1997, *ApJ*, 485, 1
- Nolta, M. R., et al. 2009, *ApJS*, 180, 296
- Nozawa, S., Itoh, N., Suda, Y., & Ohhata, Y. 2006, *Nuovo Cimento B Serie*, 121, 487
- Plagge, T., et al. 2010, *ApJ*, 716, 1118
- Press, W. H., Teukolsky, S. A., Vetterling, W. T., & Flannery, B. P. 1992, *Numerical Recipes in C: The Art of Scientific Computing*, 2nd edn. (Cambridge University Press)
- Reese, E. D., Carlstrom, J. E., Joy, M., Mohr, J. J., Grego, L., & Holzappel, W. L. 2002, *ApJ*, 581, 53
- Rephaeli, Y. 1995, *ApJ*, 445, 33
- Riess, A. G., et al. 2009, *ApJ*, 699, 539
- Rozo, E., et al. 2010, *ApJ*, 708, 645
- Sehgal, N., et al. 2010a, *ApJ*, 732, 44
- . 2010b, *ApJ*, 709, 920
- Staniszewski, Z., et al. 2009, *ApJ*, 701, 32
- Sunyaev, R. A., & Zel'dovich, Y. B. 1970, *Comments on Astrophysics and Space Physics*, 2, 66
- Swetz, D. S., et al. 2010, *ApJS*, 194, 41
- Vanderlinde, K., et al. 2010, arXiv:1003.0003
- Vieira, J. D., et al. 2010, *ApJ*, 719, 763
- Vikhlinin, A., et al. 2009, *ApJ*, 692, 1060
- Werner, N., Churazov, E., Finoguenov, A., Markevitch, M., Burenin, R., Kaastra, J. S., & Böhringer, H. 2007, *A&A*, 474, 707
- Wilson, G. W., et al. 2008, *MNRAS*, 390, 1061
- Zel'dovich, Y. B., & Sunyaev, R. A. 1969, *Ap&SS*, 4, 301

TABLE 1
ACT 2008 148 GHz SZ-SELECTED GALAXY CLUSTERS

ACT ID	RA (J2000) h m s	Dec ° ' "	SNR	θ_c (')	δT_0^a (μK)	$\delta T_0'^b$ (μK)	y_0' ($\times 10^{-4}$)	z^c	Alternative ID
All Candidates SNR > 6									
ACT-CL J0658-5557	06:58:30	-55:57:04	11.5	1.25	-483 ± 42	-734 ± 64	2.98 ± 0.26	0.30	1E0657-56 (Bullet)
ACT-CL J0638-5358	06:38:46	-53:58:45	10.0	1.25	-278 ± 28	-423 ± 42	1.68 ± 0.17	0.22	AS0592
ACT-CL J0245-5302	02:45:33	-53:02:04	9.1	1.00	-198 ± 22	-336 ± 37	1.32 ± 0.15	0.30	AS0295
ACT-CL J0102-4915	01:02:53	-49:15:19	9.0	0.75	-520 ± 58	-1046 ± 116	4.13 ± 0.46	0.75	New
ACT-CL J0438-5419	04:38:19	-54:19:05	8.0	0.50	-214 ± 27	-596 ± 74	2.35 ± 0.29	0.54	New
ACT-CL J0645-5413	06:45:30	-54:13:39	7.1	0.75	-221 ± 31	-444 ± 63	1.75 ± 0.25	0.17	A3404
ACT-CL J0546-5345	05:46:37	-53:45:32	6.5	1.75	-178 ± 27	-240 ± 37	0.95 ± 0.15	1.07	SPT-CL 0547-5345
ACT-CL J0235-5121	02:35:52	-51:21:16	6.2	4.00	-320 ± 51	-363 ± 58	1.43 ± 0.23	0.43	New
ACT-CL J0330-5227	03:30:54	-52:28:04	6.1	1.25	-145 ± 24	-221 ± 36	0.85 ± 0.14	0.44	A3128(NE)
SNR < 6 and Optically Confirmed									
ACT-CL J0616-5227	06:16:36	-52:27:35	5.9	0.50	-155 ± 26	-431 ± 73	1.70 ± 0.29	0.71	New
ACT-CL J0559-5249	05:59:43	-52:49:13	5.1	2.25	-155 ± 31	-194 ± 38	0.77 ± 0.15	0.61	SPT-CL J0559-5249
ACT-CL J0215-5212	02:15:18	-52:12:30	4.9	0.25	-140 ± 29	-801 ± 164	3.16 ± 0.65	0.51	New
ACT-CL J0509-5341	05:09:21	-53:42:05	4.8	0.50	-115 ± 24	-319 ± 67	1.27 ± 0.27	0.46	SPT-CL 0509-5342
ACT-CL J0641-4949	06:41:35	-49:48:32	4.7	0.25	-283 ± 60	-1625 ± 375	6.41 ± 1.48	0.15	A3402
ACT-CL J0232-5257	02:32:45	-52:57:08	4.7	0.25	-124 ± 26	-710 ± 152	2.80 ± 0.60	0.59	New
ACT-CL J0516-5430	05:16:30	-54:30:30	4.6	1.75	-143 ± 31	-192 ± 43	0.77 ± 0.17	0.29	AS0520/SPT-CL 0517-5430
ACT-CL J0346-5438	03:46:51	-54:38:54	4.4	1.25	-131 ± 30	-198 ± 45	0.78 ± 0.18	0.55	New
ACT-CL J0217-5245	02:17:11	-52:45:20	4.1	1.25	-98 ± 24	-150 ± 37	0.59 ± 0.14	0.34	RXC J0217.2-5244
ACT-CL J0145-5301	01:44:59	-53:01:01	4.0	1.00	-99 ± 25	-167 ± 42	0.65 ± 0.16	0.12	A2941
ACT-CL J0237-4939	02:37:03	-49:39:27	3.9	1.00	-140 ± 36	-236 ± 61	0.93 ± 0.24	0.40	New
ACT-CL J0304-4921	03:04:15	-49:21:42	3.9	1.00	-169 ± 43	-285 ± 74	1.12 ± 0.29	0.47	New
ACT-CL J0707-5522	07:07:13	-55:22:48	3.3	1.75	-218 ± 67	-293 ± 90	1.16 ± 0.35	0.43	New
ACT-CL J0528-5259	05:28:03	-52:59:53	3.1	0.50	-88 ± 28	-244 ± 78	0.94 ± 0.30	0.77	SPT-CL 0528-5300

^a The error simply reflects the SNR with no systematic uncertainty included.

^b Temperature decrement value with the effect of the ACT beam deconvolved $\delta T_0 \times C^{-1}(\theta_c)$.

^c Provided for reference: see Menanteau et al. (2010) for the sources of redshifts.

TABLE 2
CLUSTER MASS ESTIMATES

ACT ID ^a	M_{500c} ^b ($\times 10^{14} M_{\odot}$)
ACT-CL J0102-4915	9.9 ± 3.5
ACT-CL J0235-5121	6.2 ± 1.4
ACT-CL J0245-5302	6.6 ± 1.0
ACT-CL J0330-5227	9.7 ± 1.7
ACT-CL J0438-5419	12.1 ± 2.2
ACT-CL J0546-5345	5.2 ± 2.2
ACT-CL J0559-5249	5.3 ± 1.5
ACT-CL J0616-5227	6.5 ± 1.6
ACT-CL J0638-5358	9.1 ± 0.6
ACT-CL J0645-5413	7.6 ± 0.6
ACT-CL J0658-5557	14.0 ± 1.2

^a This is a subset of clusters from Table 1 with SNR > 5.

^b Masses derived from X-ray luminosities using the $M - L_X$ relation in Vikhlinin et al. (2009). The error only includes statistical error propagated from error on L_X .

APPENDIX

SELF-SIMILAR SCALING RELATION FOR $Y_0 - M$

Assuming an isothermal ICM and taking R as the radius of the cluster, the central Compton y parameter is proportional to the product of the electron temperature (T), average central electron number density (n_0), and R :

$$y_0 \propto n_0 T R. \quad (\text{A1})$$

The electron density can be related through a mean molecular weight to the gas density which, assuming a standard gas fraction, can in turn be related to the total density (ρ) of dark matter plus gas. The total density is referenced to the background critical density ($\rho \propto \rho_c$) which evolves with redshift as $E^2(z) = \Omega_M(1+z)^3 + \Omega_\Lambda$ in a flat Λ CDM universe. Furthermore, the cluster radius is a function of the mass and density such that

$$R \propto \left(\frac{M}{\rho}\right)^{1/3} \propto \left(\frac{M}{E^2(z)}\right)^{1/3}. \quad (\text{A2})$$

Under the assumptions of virialization and hydrostatic equilibrium, the temperature can be related to M and $E(z)$ (e.g., Bryan & Norman 1998):

$$T \propto M^{2/3} E^{2/3}(z). \quad (\text{A3})$$

Combining these relations, the central Compton y parameter is seen to scale with mass and redshift as

$$y_0 \propto M E^2(z). \quad (\text{A4})$$